

Effect of cations (Na⁺, K⁺, and Ca²⁺) on Methane Hydrate Formation on the External Surface of Montmorillonite: Insights from Molecular Dynamics Simulation

Yun Li, Meng Chen, Hongzhe Song, Peng Yuan, Baifa Zhang, Dong Liu, Huijun Zhou, and Hongling Bu

ACS Earth Space Chem., **Just Accepted Manuscript** • DOI: 10.1021/acsearthspacechem.9b00323 • Publication Date (Web): 19 Mar 2020

Downloaded from pubs.acs.org on March 19, 2020

Just Accepted

“Just Accepted” manuscripts have been peer-reviewed and accepted for publication. They are posted online prior to technical editing, formatting for publication and author proofing. The American Chemical Society provides “Just Accepted” as a service to the research community to expedite the dissemination of scientific material as soon as possible after acceptance. “Just Accepted” manuscripts appear in full in PDF format accompanied by an HTML abstract. “Just Accepted” manuscripts have been fully peer reviewed, but should not be considered the official version of record. They are citable by the Digital Object Identifier (DOI®). “Just Accepted” is an optional service offered to authors. Therefore, the “Just Accepted” Web site may not include all articles that will be published in the journal. After a manuscript is technically edited and formatted, it will be removed from the “Just Accepted” Web site and published as an ASAP article. Note that technical editing may introduce minor changes to the manuscript text and/or graphics which could affect content, and all legal disclaimers and ethical guidelines that apply to the journal pertain. ACS cannot be held responsible for errors or consequences arising from the use of information contained in these “Just Accepted” manuscripts.

1
2
3
4 **Effect of cations (Na⁺, K⁺, and Ca²⁺) on Methane Hydrate Formation on the**
5
6 **External Surface of Montmorillonite: Insights from Molecular Dynamics**
7
8
9 **Simulation**
10

11
12
13
14 Yun Li^{1,2} Meng Chen¹ Hongzhe Song^{1,2} Peng Yuan^{1*} Baifa Zhang^{1,2} Dong
15
16
17 Liu¹ Huijun Zhou^{1,2} Hongling Bu¹
18
19

20
21
22 1 CAS Key Laboratory of Mineralogy and Metallogeny, Guangdong Provincial Key
23
24 Laboratory of Mineral Physics and Materials, Guangzhou Institute of Geochemistry,
25
26
27 Institutions of Earth Science, Chinese Academy of Sciences (CAS), Guangzhou
28
29
30 510640, China
31

32 2 University of Chinese Academy of Sciences, Beijing 100049, China
33
34
35

36
37 ***Corresponding author:**
38

39 Prof. Dr. Peng YUAN
40

41 CAS Key Laboratory of Mineralogy and Metallogeny, Guangzhou Institute of
42
43
44 Geochemistry, Chinese Academy of Sciences (CAS),
45

46 Wushan, Guangzhou 510640, China
47

48 Tel/Fax: +86 20 85290341
49

50
51
52 E-mail address: yuanpeng@gig.ac.cn
53
54
55
56
57
58
59
60

Abstract

In this study, molecular dynamics simulations were performed to investigate the effects of montmorillonite with different surface cations (i.e., Na⁺, K⁺, and Ca²⁺) on CH₄ hydrate formation. The results showed that CH₄ hydrate cages are mainly formed beyond the montmorillonite surface. The inner-sphere adsorption of K⁺ and the outer-sphere adsorption of Na⁺ and Ca²⁺ occurred on the montmorillonite surface, leading to differences in order parameter and hydrogen bonds number of H₂O molecules. The number of structure I cages increased faster than that of structure II cages in different models, and were in agreement with the fact that CH₄ molecules can only form sI hydrate crystals. The number of 5¹² cages increased in the order: Na-Mt < Ca-Mt < K-Mt. The surface of K-Mt could promote the nucleation of CH₄ hydrate in the bulk-like solution. The above findings suggest that the coordination structure of cations on the external surface of montmorillonite plays an important role in CH₄ hydrate formation through altering the occupation of CH₄ hydrate.

Keywords:

CH₄ hydrate, montmorillonite, hydration structure, molecular dynamics simulation.

Introduction

There has been sustained interest in CH₄ hydrate due to its large energy density and environmentally abundant nature as compared to other fossil fuels (e.g., coal, oil, and natural gas) [1]. CH₄ hydrate is vastly distributed in permafrost areas and marine sediments along the continental margins under high CH₄ concentration, medium pressure, and low temperature environments [2, 3]. Structurally, CH₄ hydrate is an ice-like nonstoichiometric crystalline compound made up of CH₄ and H₂O molecules, CH₄ hydrate presents a cubic structure that consists of 46 H₂O molecules per unit cell, forming six 5¹²6² (12 pentagons and 2 hexagons) and two 5¹² cages [1, 4].

Due to the enormous potential for CH₄ hydrate to be used in energy storage and geological applications, experimental and modeling studies have focused on the nucleation and growth mechanism of CH₄ hydrate [5-7]. It has been known that the formation kinetics of CH₄ hydrate is affected by geological and environmental conditions, such as mineral type [8-11], organic matter [12-14], and inorganic salt concentration [15]. Among them, clay minerals were regarded as an important variable because they are the main component in natural sediments [10, 16-19]. According to previous studies, the formation of CH₄ hydrate in the presence of clay minerals differ from that of bulk hydrate phase, which is due to the unique structure and surface chemistry of clay minerals [16, 17]. For instance, Guggenheim et al. showed that a montmorillonite-CH₄ hydrate intercalate can be stably formed in the interlayer with a 1.2-nm interlayer distance upon pressurization at 41.4 bar. The stable upper limit of hydrate intercalate on the pressure and temperature was parallel to that of CH₄

hydrate, but the temperatures were 0.5°C–1°C lower than that of CH₄ hydrate [17]. Cha et al. showed that the large specific surface areas of clay minerals provide nucleation sites to promote the CH₄ hydrate formation, and the stable temperature and pressure range of CH₄ hydrate in the presence of clay minerals was broader than that in H₂O alone [20]. Zhou et al. observed disordered clathrate-like structures in montmorillonite-CH₄ hydrate intercalate models, and found that the behavior of CH₄ hydrate complex in the interlayer was affected by the amount of intercalated H₂O [21]. The abovementioned studies all suggest that the presence of clay minerals is a crucial variable in governing the CH₄ hydrate formation. In view of the ubiquity of clay minerals in the geological environments where CH₄ hydrate is generated, it is of no doubt that further research work is warranted to evaluate the effects of clay minerals on the CH₄ hydrate formation.

Montmorillonite is one of the most widespread clay minerals in CH₄ hydrate-bearing sediments [18-20]. Montmorillonite is a 2:1 dioctahedral clay mineral with a layer composed of an octahedral sheet sandwiched between two opposing tetrahedral sheets. The isomorphic substitutions in the tetrahedral and octahedral sheets create the negative charge of the montmorillonite layer. The layer charge is primarily balanced by alkali and alkaline earth cations adsorbed onto basal surfaces or in the interlayer region of montmorillonite [22, 23]. The role of montmorillonite in the CH₄ hydrate formation is currently a controversial subject because there are many issues that require clarification. For example, previous studies suggested that montmorillonite could promote the hydrate nucleation due to the specific surface area,

1
2
3
4 and the promotion is caused by the surface-adsorbed H₂O molecules into ordered
5
6 layers that approximate a part of hydrate lattices [6, 24]. However, some experiments
7
8 indicated that montmorillonite could inhibit gas hydrate formation by disrupting the
9
10 hydrogen bond (HB) network of H₂O molecules. Therefore, in the presence of
11
12 montmorillonite, higher pressure or a lower temperature was necessarily required to
13
14 construct hydrate structures [25, 26]. Studies on CH₄ hydrate formation in
15
16 montmorillonite suspension have revealed a unique phase equilibrium condition of
17
18 CH₄ hydrate, which was ascribed to an inhibition behavior by the capillary effect and
19
20 surface interactions of nanopores (i.e., interlayer space and interparticle space) [16, 27].
21
22 Despite the inconsistency between different studies, it has been well accepted that the
23
24 structure and surface characteristics of montmorillonite must have played important
25
26 roles in the gas hydrate formation in the natural sediments, but the underlying
27
28 mechanism requires further investigation. Cations adsorbed onto the external surface
29
30 of montmorillonite from salt solutions in an ambient environment is a crucial issue
31
32 with respect to the CH₄ hydrate formation. Previous studies have reported that a low
33
34 concentration of inorganic salts effectively promotes CH₄ hydrate formation, while a
35
36 high concentration of inorganic salts inhibits it. At a low concentration of inorganic
37
38 salts, large and polarizable anions are hydrophobic, and they will interact with
39
40 surrounding H₂O molecules to form hydrophobic hydration shells. These hydration
41
42 shells are similar to those of the hydration shells of CH₄ molecules, resulting in the
43
44 promotion of CH₄ hydrate formation [28, 29]. The inhibition of CH₄ hydrate formation
45
46 at high salt concentrations was explained by the competition between cations and CH₄
47
48
49
50
51
52
53
54
55
56
57
58
59
60

1
2
3
4 molecules for H₂O molecules, as well as the distortion in the HB structure of H₂O
5
6 molecules. It was found that smaller cations have a higher charge density, leading to
7
8 stronger electronic interactions between cations and H₂O molecules. This will cause
9
10 weak HB interactions between H₂O molecules. In contrast, large cations have a lower
11
12 charge density, leading to H₂O molecules that more easily interact with each other
13
14 through the HB network [30].
15
16
17
18

19
20 It is known that different types of inorganic salt ions (e.g., Na⁺, K⁺, Ca²⁺, Mg²⁺,
21
22 and Cl⁻) exist in the pore H₂O of CH₄ hydrate-bearing sediments [31]. The negative
23
24 charges of montmorillonite in natural sediments are compensated by the presence of
25
26 inorganic ions in pore H₂O, located on the surface and the frayed edges of
27
28 montmorillonite. The charge-dipole attraction between H₂O molecules and surface
29
30 cations results in the unique chemical and physical characteristics of the
31
32 montmorillonite surface under cation-rich environments. The distribution and
33
34 hydration characteristics of cations on the external surface determine the
35
36 hydrophilicity on the montmorillonite surface. H₂O molecules around cation on the
37
38 montmorillonite surface are chemically and physically distinct from the bulk phase.
39
40 More importantly, gas molecules introduced into the montmorillonite are interacted
41
42 with the H₂O molecules solvating cations. Therefore, an important issue is raised, i.e.,
43
44 how the external surface cations of montmorillonite influence the cage number, cage
45
46 occupancy, and distribution of CH₄ hydrate during the CH₄ hydrate formation.
47
48 Unfortunately, it is technically difficult to investigate the molecular mechanism of gas
49
50 hydrate formation on the montmorillonite surface by phase equilibrium experiments
51
52
53
54
55
56
57
58
59
60

1
2
3
4 [32, 33]. In this scenario, the development of force fields for molecular simulation of
5
6 clay minerals in recent years provides a powerful tool to study the interfacial behavior
7
8 of montmorillonite at the molecular level [34]. Particularly, molecular dynamics (MD)
9
10 simulations have been significant in studying the clay-fluid system and the gas
11
12 hydrate in the presence of clay minerals [35, 36].
13
14
15

16
17 In this study, the formation of CH₄ hydrate in the presence of montmorillonite
18
19 with different surface cations (Na⁺, K⁺, and Ca²⁺) were investigated using MD
20
21 simulations. The purpose of this study was to determine the effect of different cations
22
23 on CH₄ hydrate formation at the external surface of montmorillonite. The structure
24
25 and dynamics of H₂O molecules in different models were compared by analyzing the
26
27 density profile, radial distribution function (RDF), and mean square displacement
28
29 (MSD). The local order parameter and cage structure were investigated to gain a
30
31 better understanding of the nucleation mechanism of CH₄ hydrate on montmorillonite
32
33 surface.
34
35
36
37
38
39

40 **Methodology**

41 **Molecular models**

42
43 The molecular models of montmorillonite were derived from the pyrophyllite
44
45 structure [37], which was obtained from the American Mineralogist Crystal Structure
46
47 Database [38]. The lattice parameters of the unit cell of pyrophyllite are: $a = 5.16 \text{ \AA}$, b
48
49 $= 8.97 \text{ \AA}$, and $c = 9.37 \text{ \AA}$, and $\alpha = 91.5^\circ$, $\beta = 100.46^\circ$, and $\gamma = 89.6^\circ$. To prepare the
50
51 montmorillonite model, the layer charge was created primarily by the substitution of
52
53 Mg²⁺ for Al³⁺ in the octahedral sheet, and the isomorphic substitutions obey
54
55
56
57
58
59
60

Loewenstein's rule (i.e., two substitution sites cannot be adjacent) [39]. The Na⁺, K⁺, and Ca²⁺ were used to balance the negative layer charge. Thus, the chemical formula of montmorillonite is M[Al₃Mg][Si₈O₂₀](OH)₄, with M = Na⁺, K⁺, and Ca²⁺. A 6×4×1 supercell model with $l_x = 3.096$ nm and $l_y = 3.586$ nm was created. The final orthorhombic model was obtained from the triclinic supercell model, which would not affect the simulation results [40, 41]. Three montmorillonite models with different surface cations (i.e., 24 Na⁺, 24 K⁺, and 12 Ca²⁺) were created. A bulk solution model was generated including 140 CH₄ and 1610 H₂O molecules, which were randomly distributed within a 3.096 nm × 3.586 nm × 5 nm simulation box. The CH₄ molar fraction was 0.08 in this study, about half of that in CH₄ hydrate crystal, and thus not all the H₂O molecules could convert into CH₄ hydrate. Additionally, the CH₄ molar fraction satisfied the condition that the CH₄ molecules would remain uniformly distributed in the liquid H₂O without phase separation [42, 43]. Then, the bulk solution model was added onto the montmorillonite sheet. Three models with different cations were abbreviated as Na-Mt, K-Mt, and Ca-Mt. Simulation for the different models were repeated at three times independently, which were recorded as Run 1, Run 2, and Run 3, respectively. The initial configuration of the simulation model is illustrated in Figure 1.

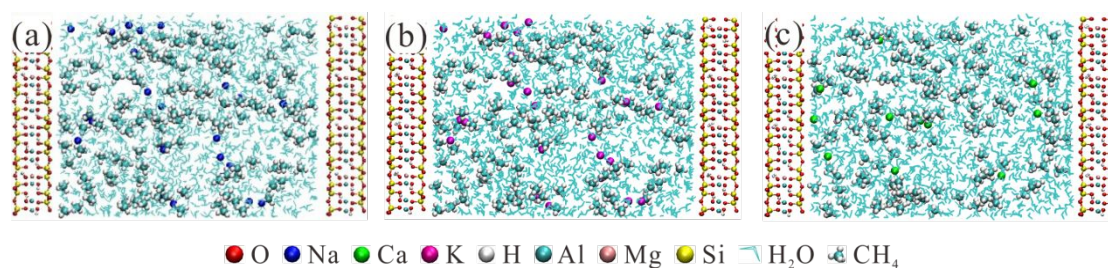


Figure 1. Initial configuration of the simulation models. (a) Na-Mt, (b) K-Mt, (c) Ca-Mt. The

1
2
3
4 stick framework represented the montmorillonite layer.
5

6 **Force field and simulation details**

7
8
9 All the MD simulations were performed with the GROMACS package (version
10 5.1.2) [44]. Montmorillonite was modeled by the ClayFF force field [45]. The optimized
11 potentials for liquid simulations all-atom (OPLS-AA) force field was used for CH₄
12 molecules [46]. TIP4P-Ice model was used for H₂O and the settle algorithm was
13 employed to constrain the rigid geometry of H₂O molecules [47]. The equation of
14 motion was integrated with the leapfrog algorithm and with a time step of 1.0 fs.
15 Lorentz-Berthelot combining rules were applied to calculate the Lennard-Jones
16 potentials between different atoms. Short-range non-bonded interactions were cutoff
17 at 1.25 nm [48]. The particle-mesh Ewald (PME) method was used to calculate the
18 long-range electrostatic interactions with a Fourier spacing of 0.12 nm [49].
19
20
21
22
23
24
25
26
27
28
29
30
31
32
33

34
35 In each MD simulation, energy minimization was performed to relax the initial
36 configuration with the steepest-descent algorithm at first. After energy minimization,
37 0.2 ns of isothermal-isobaric (*NpT*) ensemble simulation was employed for
38 equilibration under 250 K and 50 MPa, the Berendsen coupling method was used to
39 control temperature and pressure with a time constant of 0.1 ps and 0.5 ps,
40 respectively. Subsequently, the equilibrated configuration was simulated in *NpT*
41 ensemble at the same temperature and pressure for 1000 ns, but temperature was
42 controlled using the Nosé-Hoover thermostat [50] with a time constant of 1 ps, and
43 pressure was controlled using the Parrinello-Rahman barostat [51] with a time constant
44 of 4 ps. This temperature and pressure can provide sufficient driving force for
45
46
47
48
49
50
51
52
53
54
55
56
57
58
59
60

attaining faster growth kinetics of CH₄ hydrate during the simulation [43, 52, 53]. Only the *z* dimension was scaled in *NpT* simulations. Periodic boundary conditions were imposed on the molecular structures in three directions [54].

Data analysis

Order parameter

The tetrahedral order parameter (F_3) [55] and four-body order parameter (F_4) [56, 57] were used to analyze the H₂O structure, and these were defined as follows (Eqs. (1) and (2)):

$$F_3 = \left\langle \sum_{j=1}^{n_i-1} \sum_{k=j+1}^{n_i} \left(|\cos \theta_{jik}| \cos \theta_{jik} + \cos^2(109.47^\circ) \right)^2 \right\rangle \quad (1)$$

where θ_{jik} denotes the angle between the specified oxygen i_{th} atom and the other two oxygen j_{th} and k_{th} atoms within a distance of 0.35 nm around the i_{th} atom; n_i denotes the number of oxygen atoms. Average $\langle \dots \rangle$ are computed over all H₂O molecules. The average values of the F_3 parameter remain at approximately 0.1 for liquid H₂O and 0.01 for solid H₂O (including CH₄ hydrate and ice).

$$F_4 = \frac{1}{n} \sum_{i=1}^n \cos 3\phi_i \quad (2)$$

where ϕ_i denotes the dihedral angle between the oxygen atoms of two adjacent molecules and the outermost hydrogen atoms, and n indicates the number of the oxygen atom pairs of H₂O molecules within 0.35 nm. The average values of F_4 are -0.04, -0.4, and 0.7 for H₂O, ice, and CH₄ hydrate, respectively.

Cage structure

The structure of H₂O was identified by searching for oxygen atoms within 0.61 nm around CH₄ molecules. The topological structure of the ring formation was

determined by the connection of the H₂O molecules. Two oxygen atoms were deemed connected if their distance was less than 0.35 nm. Then, all the possible pentagonal and hexagonal rings formations were identified via connected oxygen atoms. Oxygen atoms were utilized as the vertices to identify the 5¹², 5¹²6², 5¹²6³, and 5¹²6⁴ cages composed of 20, 24, 26, and 28 H₂O molecules, respectively [43, 58, 59].

Results and discussion

Order parameter and cage structural analysis

The order parameter and cage structure were investigated to study the nucleation and growth events of CH₄ hydrate. Figure 2 shows the evolution of order parameter (F₃ and F₄) in different simulation models for run 3 (when averaged over all H₂O molecules). The plots of order parameter of all H₂O molecules in different simulation models for run 1 and run 2 are in Figure S1.

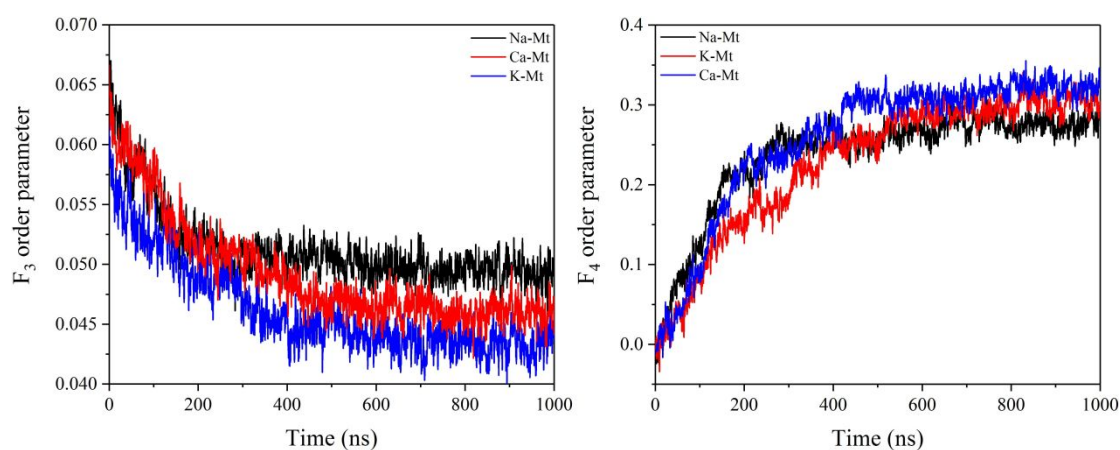
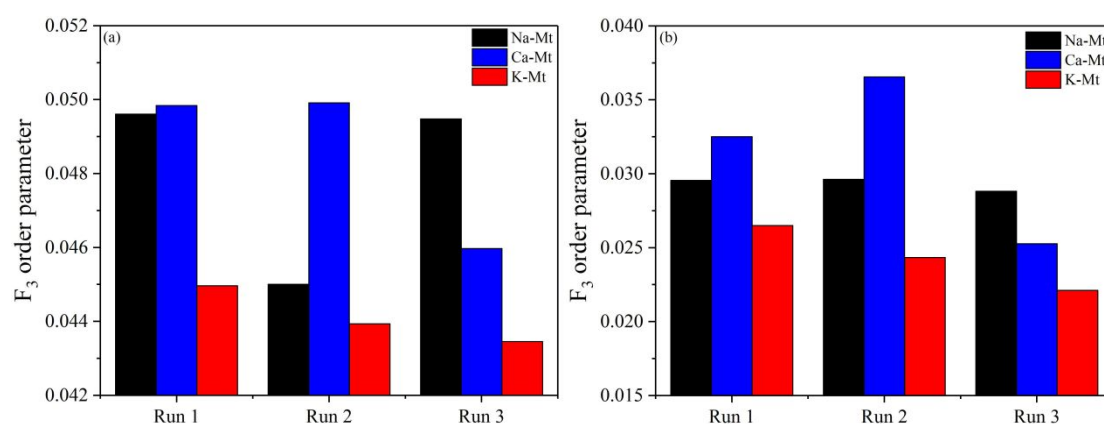


Figure 2. Evolution of order parameter in the different simulation models for run 3.

As shown in Figures 2 and S1, the decrease in F₃ and the increase in F₄ indicated the nucleation and growth process of the CH₄ hydrate, and the trend in order parameters demonstrated the transformation from a disordered state (liquid H₂O) to an ordered state (CH₄ hydrate). Compared with the F₃ and F₄ for different simulation

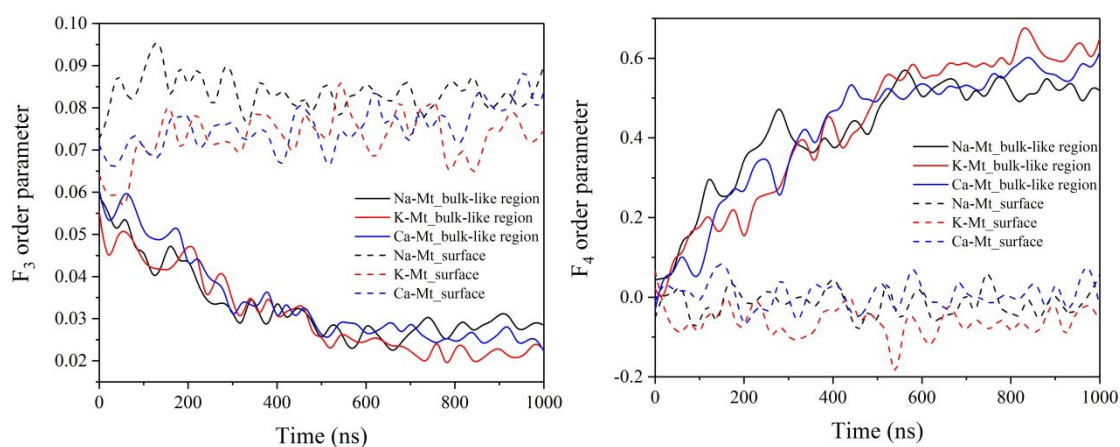
1
2
3
4 models, the sharp changes in F_3 and F_4 indicated the rapid growth of CH_4 hydrate
5
6 during 200–600 ns. After 600 ns, either F_4 or F_3 reached a steady value, which
7
8 indicated that the growth of CH_4 hydrate almost finished, and a large number of CH_4
9
10 hydrate cages formed. The equilibrium values of F_3 and F_4 are between that of liquid
11
12 H_2O and CH_4 hydrate, reflecting part of liquid H_2O was also present. It was expected
13
14 that H_2O molecules cannot be completely converted into CH_4 hydrate because the
15
16 $\text{CH}_4/\text{H}_2\text{O}$ ratio was approximately 0.08 in this study. Additionally, the nucleation and
17
18 subsequent growth of CH_4 hydrate results in a significant drop in potential energy
19
20 during the simulation (Figure S2). The average values of F_3 order parameter in
21
22 different simulation models during 800-1000 ns for run 1-3 are listed in Figure 3a.
23
24 There was little difference in the equilibrium values of F_3 in different montmorillonite
25
26 models after CH_4 hydrate formation. The lower value of F_3 in the K-Mt model
27
28 indicated that a more optimal tetrahedral structure of H_2O molecules was formed.
29
30
31
32
33
34
35
36



37
38
39
40
41
42
43
44
45
46
47
48
49
50
51 **Figure 3** Average value of F_3 order parameter in different simulation models during 800-1000 ns
52 for run 1-3. (a) All H_2O molecules. (b) H_2O molecules in the bulk-like region.
53
54

55
56 To analyze the effect of the external surface of montmorillonite on CH_4 hydrate
57
58 formation, the evolution of both parameters in the bulk-like region (3.25-3.75 nm) and
59
60

1
2
3
4 surface (the first adsorbed H₂O layer, < 1.27 nm) was also investigated (Figures 4 and
5
6
7 S3). In Figures 4 and S3, the value of F₄ and F₃ of H₂O molecules in the bulk-like
8
9 region approached the value of the hydrate phase, which indicated that hydrate cages
10
11 were formed beyond the montmorillonite surface. F₃ and F₄ of H₂O molecules on the
12
13 montmorillonite surface approached the values of liquid H₂O, which might be due to
14
15 the influence of cation hydration on the HB networks of H₂O structures, resulting in
16
17 the liquid arrangement of H₂O molecules. Compared with Na-Mt and Ca-Mt, the
18
19 lower F₃ value of H₂O molecules in the bulk-like region of K-Mt model signified that
20
21 it was favorable to form optimal tetrahedral structure of H₂O molecules in K-Mt
22
23 (Figure 3b). Therefore, the surface of K-Mt promoted the nucleation of CH₄ hydrate
24
25 in the bulk-like region, while the surface and the bulk-like region of Ca-Mt and
26
27 Na-Mt does not show obvious promotion of CH₄ hydrate nucleation. In general, the
28
29 surface of K-Mt model could significantly promote the nucleation of CH₄ hydrate
30
31 in the bulk-like solution. The bulk-like region in K-Mt was easier to form CH₄ hydrate
32
33 cages than that in the Ca-Mt and Na-Mt.
34
35
36
37
38
39
40
41



57 **Figure 4.** Evolution of order parameter for run 3 at the montmorillonite surface and the bulk-like
58 region in different simulation models.
59
60

1
2
3
4 To quantitatively disclose the evolution of hydrate cages during CH₄ hydrate
5 formation, four different types of cage structures (i.e., 5¹², 5¹²6², 5¹²6³, and 5¹²6⁴)
6 were identified by using the cage analysis algorithm. Figures 5 and S4 show the
7 evolution of cage structures in different simulation models during the simulation. The
8 snapshot of cage structures at different simulation times shows the stages of
9 nucleation and growth of CH₄ hydrate, which are illustrated in Figures 6 and S5.
10
11
12
13
14
15
16
17
18
19
20
21
22
23
24
25
26
27
28
29
30
31
32
33
34
35
36
37
38
39
40
41
42
43
44
45
46
47
48
49
50
51
52
53
54
55
56
57
58
59
60

Figures 5 and S4 show that 5¹² cages were first formed in the bulk-like solution, and the nucleation time (when the first stable cage structure formed) was different in different montmorillonite models, which was consistent with previous work that indicated that the nucleation process of hydrate tends to be more stochastic in terms of cage type and nucleation time [60-63]. The appearance of hydrate cages in the bulk-like region of the model was attributed to the locally high concentration of CH₄ molecules [64]. It was observed that the 5¹²6², 5¹²6³, and 5¹²6⁴ cages gradually appeared with increasing simulation time. The formation rates of the 5¹² and 5¹²6² cages were higher than those of the 5¹²6³ and 5¹²6⁴ cages, which indicated that the formation of the 5¹² and 5¹²6² cages was strongly correlated during the simulation. A small number of 5¹²6⁴ cages in these models implied that it was difficult for CH₄ molecules to effectively stabilize the 5¹²6⁴ cages due to the molecular size of CH₄ molecule [52]. After CH₄ hydrate formation in different models, an amorphous crystal was finally obtained (Figure 6). Both structure I (sI) (5¹² and 5¹²6² cages) and structure II (sII) (5¹² and 5¹²6⁴ cages) geometries were observed. The number of sI structures increased much faster than the number of sII structures with the CH₄ hydrate growth.

Consequently, it can be said that the sI hydrate predominates. This result was in agreement with the fact that CH₄ can form only sI hydrate in nature [1]. Particularly, the number of 5¹² cages in K-Mt was more than that in Ca-Mt and Na-Mt at the equilibrium stage. It was due to the hydration structure of cations in different models, leading to difference in CH₄ hydrate formation. The cage ratio is defined as the ratio of 5¹²6² cages with respect to 5¹² cages. The cage ratio in different simulation models from 0.2 to 0.6 were significantly lower than the CH₄ hydrate structure (cage ratio =3) [65]. Additionally, the ratios were also consistent with previous reported that the cations of montmorillonite affect the occupancy inside small cages of CH₄ hydrate [66].

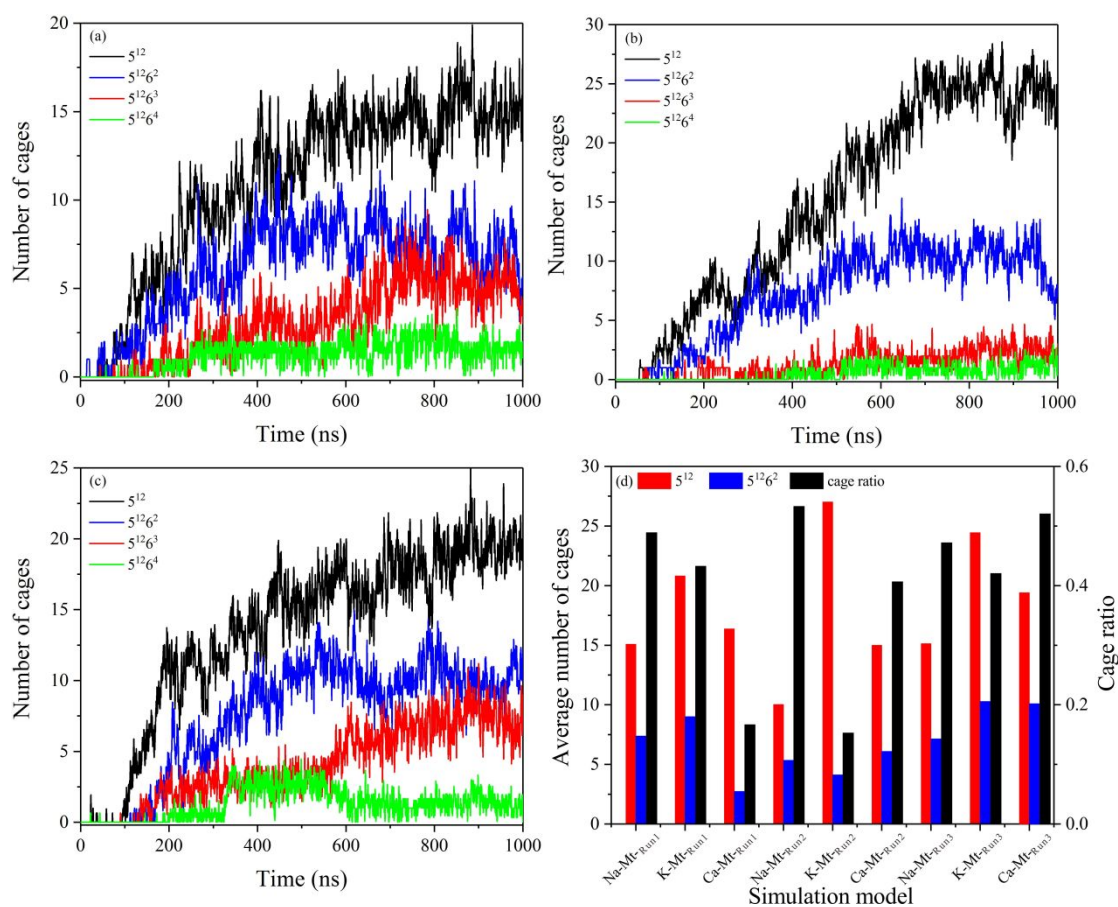


Figure 5. Evolution of the number of cages in different simulation models for run 3. (a) Na-Mt.

(b) K-Mt. (c) Ca-Mt. (d) The number of 5^{12} and $5^{12}6^2$ cages averaged over the last 50 ns. The cage ratio of the average number of $5^{12}6^2$ to 5^{12} cages was also shown.

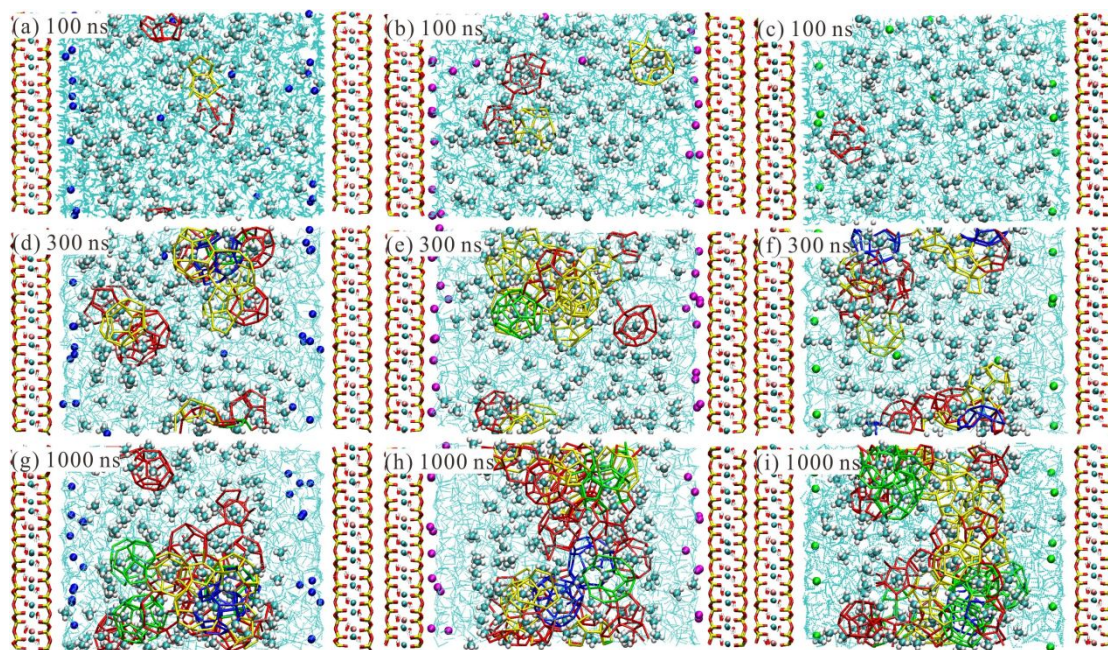


Figure 6. Snapshots of the CH_4 hydrate cages at different times in different simulation models for run 3. (a, d, and g) Na-Mt. (b, e, and h) K-Mt. (c, f, and i) Ca-Mt. CH_4 hydrate cages were shown with different colors: red for 5^{12} , yellow for $5^{12}6^2$, green for $5^{12}6^3$ and blue for $5^{12}6^4$.

Moreover, CH_4 hydrate formation was further supported by the RDF and coordination number (CN) of oxygen atom (OW) in H_2O and around carbon atom (C) in the CH_4 . The RDF for component B around A is defined as

$$g_{A-B}(r) = \frac{dN_{A-B}}{dr} \frac{1}{4\pi\rho_B r^2}, \text{ where } \rho_B \text{ is the average density of components B,}$$

dN_{A-B} is the average number of components B around A between the region of r and $r+dr$, and CN of B around A was obtained from the integral of the RDF profile from the position starting at $r = 0$ to the position of the first minimum located after the first peak [48]. In Figure 7, the first peak of $g_{\text{C-OW}}(r)$ appeared at approximately 0.386 nm and was in a good agreement with the neutron diffraction results and pair correlation

1
2
3
4 functions for CH₄ hydrate [67]. The CNs of H₂O molecules around the CH₄ in the
5
6 Na-Mt, K-Mt, and Ca-Mt models were 22.50, 22.53, and 22.63, respectively. These
7
8 results were in good agreement with those of the fully formed CH₄ hydrate in
9
10 previous work [67]. In addition, Figure S6 illustrates the RDFs of C-C and OW-OW
11
12 during three segments of simulation trajectories (0–100 ns, 400–500 ns, and 900–
13
14 1000 ns). A strong peak of $g_{C-C}(r)$ occurred at approximately 0.384 nm during 0–100
15
16 1000 ns). A strong peak of $g_{C-C}(r)$ occurred at approximately 0.384 nm during 0–100
17
18 ns, which indicated that the CH₄ molecules were distributed in contact with each other
19
20 in the liquid phase. Then, the peak at 0.384 nm almost disappeared, and a strong peak
21
22 merged at approximately 0.648 nm during 900–1000 ns, which was consistent with
23
24 the distance between CH₄ molecules in the bulk CH₄ hydrate phase [68, 69]. The third
25
26 peak appeared at approximately 1.05 nm, but it also exhibited a small and broad peak
27
28 at 0.39 nm. All the results demonstrated that CH₄-CH₄ molecular interactions
29
30 occurred across the hydrate structures during the CH₄ hydrate formation. The
31
32 $g_{OW-OW}(r)$ function is defined as the oxygen-oxygen distance between two H₂O
33
34 molecules. Among all montmorillonite models, the first, second, and third peaks of
35
36 $g_{OW-OW}(r)$ appeared at approximately 0.28 nm, 0.45 nm, and 0.65 nm, respectively.
37
38 This result was consistent with that of stable bulk CH₄ hydrate [68], indicating that the
39
40 H₂O molecules were arranged in clathrate-like structures.
41
42
43
44
45
46
47
48
49
50
51
52
53
54
55
56
57
58
59
60

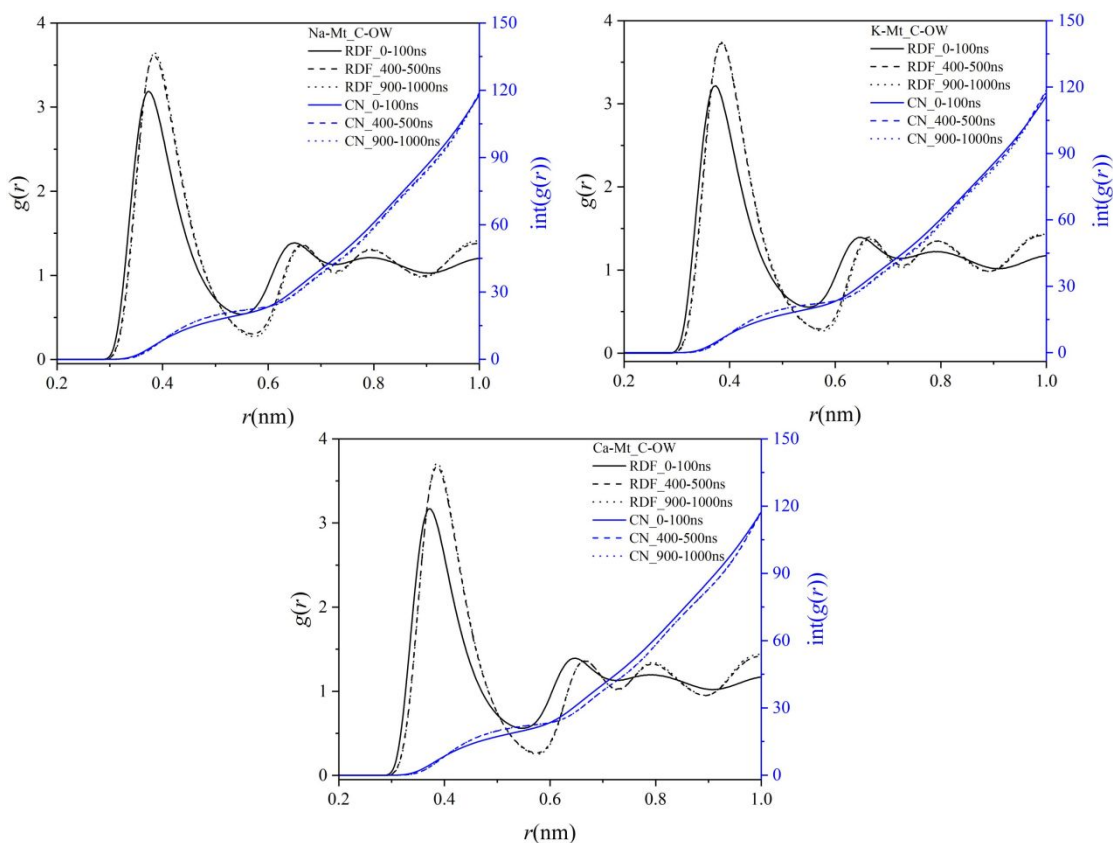


Figure 7. Radial distribution function of the OW around the C in different simulation models for run 3. OW and C represented the oxygen atom of H_2O and carbon atom of CH_4 , respectively.

Density profile of different components

To investigate the interaction of cations, CH_4 , and H_2O molecules with the montmorillonite surface, the distributions of different components, perpendicular to the montmorillonite sheets, were calculated. The snapshot of cation distribution in different simulation models is shown in [Figure S7](#). The density profile of different components is shown in [Figure 8](#).

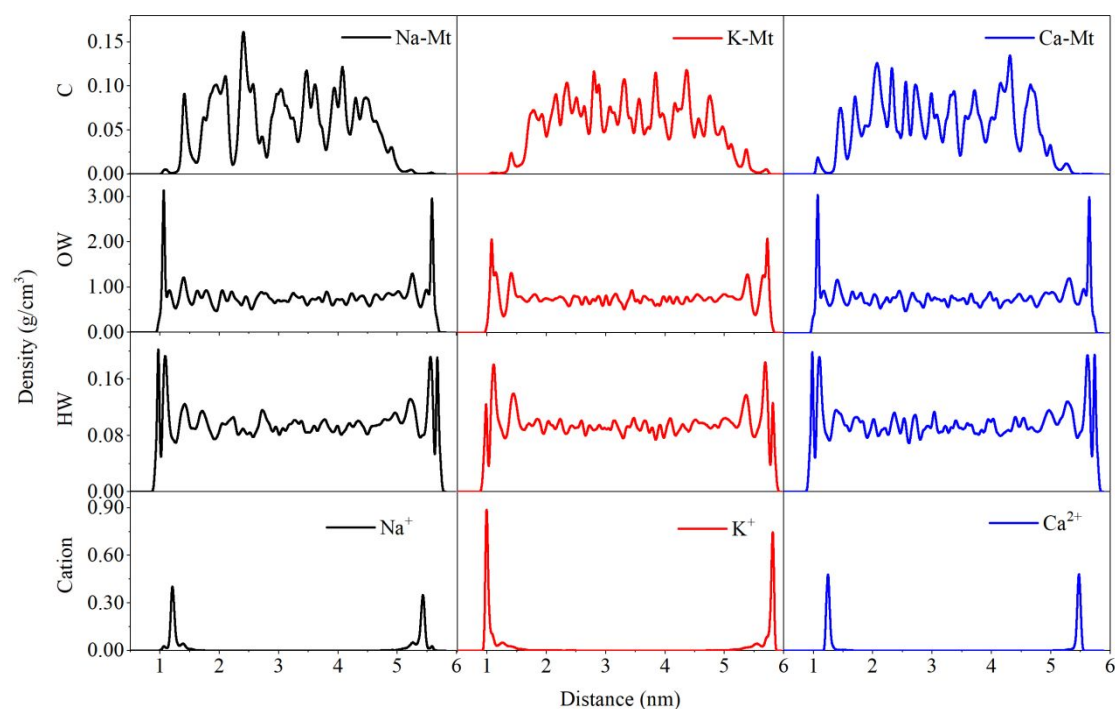


Figure 8. Density profile of different components along z direction for run 3. HW represented the hydrogen atom of H_2O .

The density profile was averaged over the simulation trajectory from 600 to 1000 ns. In Figure 8, a large amount of CH_4 molecules was distributed in the bulk-like region. The H_2O distribution was symmetric with two peaks on both sides. OW of the first adsorbed H_2O layer was located at distances of 0.94–1.26 nm, 0.96–1.28 nm, and 0.94–1.27 nm above the Na-Mt, K-Mt, and Ca-Mt surfaces, respectively. HW of the first adsorbed H_2O layer was located at distances of 0.87–1.01 nm, 0.88–1.03 nm, and 0.87–1.03 nm above the Na-Mt, K-Mt, and Ca-Mt surfaces, respectively. The position of OW and HW demonstrated the orientation of H_2O molecules in the first adsorbed H_2O layer. The density of adsorbed H_2O layer in Na-Mt and Ca-Mt was approximately 3.0 g/cm^3 , while that in K-Mt was approximately 2.0 g/cm^3 . The subtle differences in H_2O density were attributed to the adsorption behavior of cations on the montmorillonite surface. The Na^+ , K^+ , and Ca^{2+} were mainly located at distances of

1.11–1.32 nm, 0.92–1.17 nm, and 1.17–1.4 nm, respectively. The K^+ was distributed closer to the surface than Na^+ and Ca^{2+} . Na^+ and Ca^{2+} were distributed predominantly in the outer-sphere. However, K^+ was distributed in the vacancies of the hexagonal rings of the Si-O tetrahedron, where they formed an inner-sphere adsorption, and the basal oxygen atoms (OB) also contributed to their first hydration shell (Figure 9).

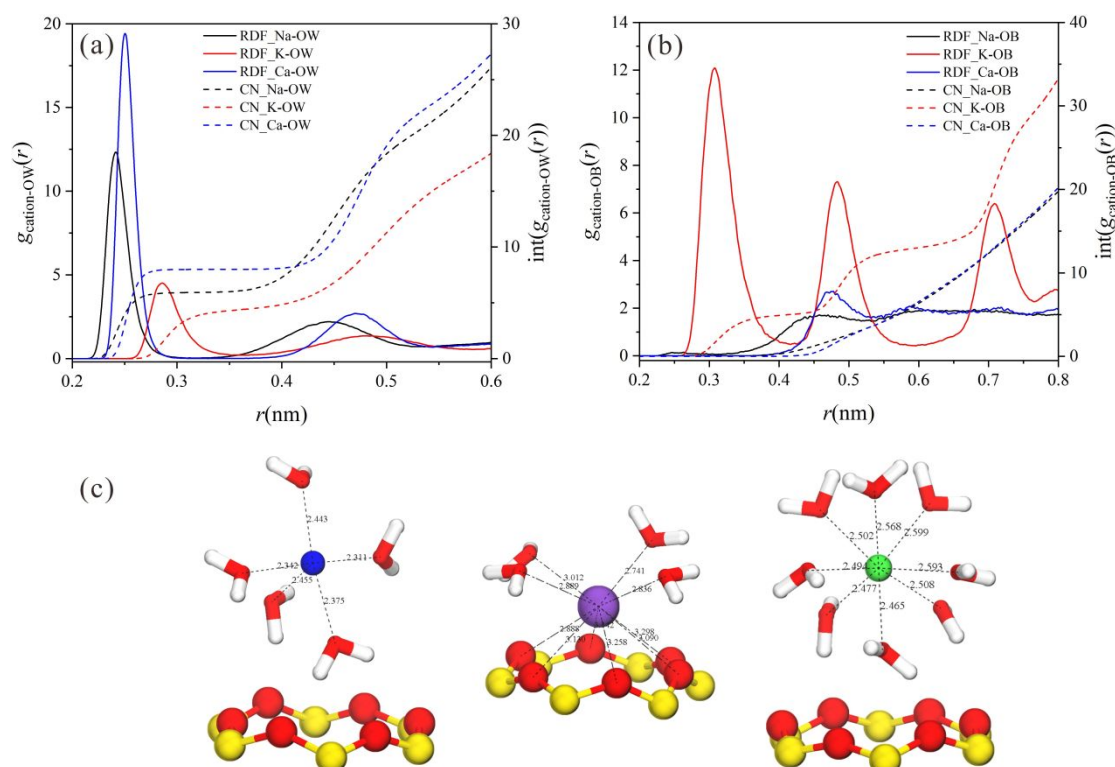


Figure 9. Radial distribution function of cation-OW (a) and cation-OB (b) in different simulation models for run 3. (c) From left to right: hydration structure of Na⁺, K⁺, and Ca²⁺ cations, respectively. Na⁺, K⁺, and Ca²⁺ are shown as blue ball, violet ball, and green ball, respectively.

The hydration characteristics of Na⁺, K⁺, and Ca²⁺ were consistent with the findings of previous research [70, 71]. Figure 9a-b provide the RDFs of $g_{\text{cation-OW}}(r)$ and $g_{\text{cation-OB}}(r)$ during the last 10 ns. The first peak of $g_{\text{cation-OW}}(r)$ in Na-Mt, K-Mt, and Ca-Mt appeared at approximately 0.242 nm, 0.288 nm, and 0.25 nm, respectively, (Figure 9a), which represent the hydration radii of Na⁺, K⁺, and Ca²⁺, respectively.

1
2
3
4 The intensity of the first peak and the hydration radius of different cations in the
5
6 $g_{\text{cation-ow}}(r)$ curves indicated the different hydration abilities and hydration enthalpies
7
8 of these cations, which were consistent with previous results [72]. However, as for the
9
10 distribution of K^+ on the montmorillonite surface, part of the oxygen coordination was
11
12 provided by the OB, where the first peak of $g_{\text{cation-OB}}(r)$ in K-Mt appeared at
13
14 approximately 0.31 nm (Figure 9b). The CN of OB around the K^+ was approximately
15
16 5.034, while the contribution of OB was close to zero for Na^+ and Ca^{2+} . Note that the
17
18 total CNs of Na^+ , K^+ , and Ca^{2+} were 5.928, 7.993, and 10.493, respectively. In
19
20 general, the cation hydration on the montmorillonite surface alters the number of H_2O
21
22 molecules involved in the CH_4 hydrate formation. Additionally, the number of CH_4
23
24 molecules decreased near the montmorillonite surface due to the salting-out effect,
25
26 which reduced the solubility of CH_4 molecules in the solution caused by Na^+
27
28 hydration, and increased the propensity of CH_4 molecules to be adsorbed on the
29
30 hydrate surface [73, 74]. The $g_{\text{cation-C}}(r)$ also supported this result from Figure S8, which
31
32 shows that the intensity of RDF peaks for CH_4 around Na^+ , K^+ , and Ca^{2+} decreased
33
34 during CH_4 hydrate formation. The cations near the montmorillonite surface would
35
36 disrupt the HB structures of interfacial H_2O molecules, which might affect the hydrate
37
38 formation in the bulk-like region. Thus, the effect of the external surface of
39
40 montmorillonite on CH_4 hydrate formation depending on the hydration properties of
41
42 different surface cations.
43
44
45
46
47
48
49
50
51
52
53
54

55 ***Hydrogen bond structural analysis***

56 The H_2O molecules in the CH_4 hydrate are connected by HBs. The HB networks
57
58
59
60

1
2
3
4 are frequently formed and broken during CH₄ hydrate formation. It is important to
5
6 assess the number and length of HB structure at different regions of the simulation
7
8 models during CH₄ hydrate formation. The first strong peaks of $g_{\text{OB-HW}}(r)$ and
9
10 $g_{\text{OW-HW}}(r)$ both appeared at approximately 0.184 nm (Figure S9), which was close to
11
12 the HB distance of H₂O molecules in hydrate cages. From Figure S10a-b, the average
13
14 number of HBs in the Na-Mt and Ca-Mt models was almost identical. The average
15
16 number of HBs per H₂O molecule and the average number of HBs per H₂O molecule
17
18 contributing to other H₂O molecules in K-Mt model was apparently greater than that
19
20 of the Na-Mt and Ca-Mt models, which implied that the arrangement of H₂O
21
22 molecules in the K-Mt model was more regular than that in the Ca-Mt and Na-Mt
23
24 models. Hence, these results demonstrated that the average number of HBs per H₂O
25
26 molecule in the models was approximate to the number in the bulk solid H₂O phase
27
28 [75, 76], illustrating the formation of the hydrate phase. As expected, due to the
29
30 inner-sphere adsorption behavior of K⁺ cations on the montmorillonite surface, the
31
32 average number of HBs per H₂O molecule contributing to the Si-O tetrahedral in
33
34 K-Mt was slightly lower than that of the Na-Mt and Ca-Mt models (Figure S10c).
35
36 Therefore, compared with the Na-Mt and Ca-Mt models, a small number of H₂O
37
38 molecules was involved in the formation of HBs on the K-Mt surface, and the K⁺
39
40 cations of K-Mt had little effect on the CH₄ hydrate formation in the bulk-like region.
41
42
43
44
45
46
47
48
49
50
51

52 53 **Diffusion coefficient of H₂O molecules**

54
55 To access the reliability of the diffusion properties of H₂O molecules during CH₄
56
57 hydrate formation, the self-diffusion coefficient D of different components was
58
59
60

1
2
3
4
5
6
7
8
9
10
11
12
13
14
15
16
17
18
19
20
21
22
23
24
25
26
27
28
29
30
31
32
33
34
35
36
37
38
39
40
41
42
43
44
45
46
47
48
49
50
51
52
53
54
55
56
57
58
59
60

calculated as follows: $\frac{1}{N} \sum_{i=1}^N \left\langle \left| \mathbf{r}_i^{\mathbf{u}}(t) - \mathbf{r}_i^{\mathbf{u}}(0) \right|^2 \right\rangle = 2dtD$, where N denotes the number of atoms of the selected components, $\mathbf{r}_i^{\mathbf{u}}(t)$ denotes the center-of-mass position of the i_{th} atom at time t , and d indicates the diffusion dimension (*i.e.*, $d=3$ for the total self-diffusion coefficient). The left-hand side is usually termed as the MSD [48, 77].

Figure S11 illustrates the MSD profile of H₂O molecules in different simulation models during the last 10 ns for run 3. The MSD profiles of H₂O molecules were fitted for calculating the self-diffusion coefficients, which are 0.96×10^{-7} cm²/s for Na-Mt, 1.33×10^{-7} cm²/s for K-Mt and 0.98×10^{-7} cm²/s for Ca-Mt. Therefore, the self-diffusion of H₂O molecules in Na-Mt and Ca-Mt was basically identical and less than that in K-Mt. The possible reasons for this result are as follows. On the one hand, the formation of hydrate decrease the diffusion coefficient of H₂O molecules. On the other hand, the presence of cations on the external surface of montmorillonite lead to the difference in cage number, resulting in the different diffusion coefficients of H₂O molecules. Thirdly, the coordination structure of cation could also restrict the diffusion of H₂O molecules.

The above simulation results show that the CH₄ hydrate formation differs in the montmorillonite with different surface cations due to the effects of the coordination structure of cation. The balance between cation/surface, cation/H₂O, and H₂O/surface interactions controlled the structural complexes on the montmorillonite surface. The size and the charge amount of cations on the surface significantly influenced the CH₄ hydrate formation by altering the cage occupancy of CH₄ hydrate. In the nucleation stage, the hydrate cages were formed in the bulk-like solution due to the local high

1
2
3
4 CH₄ concentration. The hydrate nucleus grew in the bulk-like solution and the number
5
6 of HBs per H₂O molecules gradually increased. During the growth stage, the
7
8 population of sI structures increased much faster than that of the sII structure. This
9
10 result suggests that the nucleus of CH₄ hydrate in montmorillonite models mainly
11
12 grows into an sI crystal, which was in accordance with the fact that CH₄ molecules
13
14 can only form sI hydrate. In addition, the number of 5¹² cages in K-Mt was more than
15
16 that in Ca-Mt and Na-Mt, resulting in different of hydrate formation on the external
17
18 surface of montmorillonite with different cations.
19
20
21
22
23
24

25 In natural gas hydrate-bearing sediment environments, the content and surface
26
27 cations of montmorillonite vary for different sedimentary basins [18, 19, 35]. Generally
28
29 speaking, the pore H₂O in the sediment contains Na⁺, K⁺, Ca²⁺, Cl⁻, and SO₄²⁻ ions,
30
31 which originated from the ocean H₂O deep brine [78]. Such pore H₂O resulted from the
32
33 mixing of seawater with the fluids released from the dehydration and illitization
34
35 reactions involving smectite in-depth [35]. The cations in pore H₂O readily exchange
36
37 with cations from the montmorillonite surface or are attracted by the defects on the
38
39 surface, generating montmorillonite with different surface cations. The present work
40
41 shows that the hydration of cations affected the formation and distribution of CH₄
42
43 hydrate beyond the montmorillonite surface. The surface of K-Mt could promote the
44
45 nucleation of CH₄ hydrate in the bulk-like solution. The findings implied that the
46
47 effect of surface cations of montmorillonite on CH₄ hydrate formation should be
48
49 considered in montmorillonite-rich sedimentary basins. Therefore, the natural gas
50
51 hydrate reservoir with higher montmorillonite content might effectively inhibit
52
53
54
55
56
57
58
59
60

1
2
3
4 secondary hydrate formation during CH₄ production, and thus, should be considered
5
6 for such results in natural gas hydrate development.
7
8

9 Furthermore, the ability of the inhibition effect of montmorillonite on CH₄
10 hydrate formation has significant implications for the formation of hydrate plugs in
11 the wellbore during the deepwater drilling. Two major problems with CH₄ hydrate are
12 generated in deepwater drilling with H₂O-based drilling muds [25]. On one hand, the
13 hydrate may form plug in the wellbore to prevent drill string rotation due to the
14 mechanical strength of a large mass of hydrates. On the other hand, the loss of a large
15 number of H₂O molecules from the drilling mud severely influences the mud fluidity.
16
17 In the most extreme scenario, all solid particles will settle out in the wellbore.
18
19 Therefore, it is hoped that montmorillonite could effectively prevent CH₄ hydrate
20 formation in deepwater drilling.
21
22
23
24
25
26
27
28
29
30
31
32
33
34

35 **Conclusions**

36
37 Molecular dynamic simulation was performed to examine the formation process
38 of CH₄ hydrate with different cations (Na⁺, K⁺, and Ca²⁺) located on the external
39 surface of montmorillonite. According to the results obtained, the nucleus grows in
40 the bulk-like solution to form 5¹², 5¹²6², 5¹²6³, and 5¹²6⁴ cages. The number of sI
41 structure increased faster than that of the sII structure. The cations exhibited a
42 monolayer adsorption configuration with inner-sphere (K⁺) and outer-sphere (Na⁺ and
43 Ca²⁺) hydration behavior on the montmorillonite surface, resulting in different
44 coordination structures with surface cations. As a result, CH₄ molecules cannot break
45 through the hydration layer to form CH₄ hydrate near the surface. The arrangement of
46
47
48
49
50
51
52
53
54
55
56
57
58
59
60

1
2
3
4 H₂O molecules in K-Mt exhibited a more optimal tetrahedral structure than that in the
5
6 Ca-Mt and Na-Mt surface, indicating that the K-Mt surface could promote the
7
8 nucleation of CH₄ hydrate in the bulk-like solution as compared to that of the Ca-Mt
9
10 and Na-Mt surfaces. Additionally, the number of 5¹² cages decreased in the order:
11
12 Na-Mt < Ca-Mt < K-Mt. Therefore, this study notes that the existence of cations on
13
14 the surface of montmorillonite plays a key role in controlling CH₄ hydrate formation
15
16 through altering the cage occupancy of the CH₄ hydrate. These findings are
17
18 significant not only for understanding the formation mechanism of CH₄ hydrate in
19
20 natural sediments with abundant montmorillonite, but also for its potential application
21
22 in inhibiting the CH₄ hydrate formation in deepwater drilling and natural gas hydrate
23
24 development.
25
26
27
28
29
30
31
32
33
34

35 **Acknowledgments**

36
37 This work was supported by National Special Support for High-Level Personnel
38
39 and Youth Innovation Promotion Association CAS for the excellent members
40
41 (2016-81-01), National Natural Science Foundation of China (Grant Nos. 41472044,
42
43 41272059, and 41602034), This is a contribution (No. IS-XXX) from GIGCAS.
44
45
46
47
48
49
50
51
52
53
54
55
56
57
58
59
60

References

- [1] Sloan, E. D.; Carolyn, A. K. Clathrate Hydrates of Natural Gases. *Taylor & Francis. 3rd ed.* **2007**, 60-61.
- [2] Jager, M. D.; Sloan, E. D. The effect of pressure on methane hydration in pure water and sodium chloride solutions, *Fluid Phase Equilib.* **2001**, *185*, 89-99.
- [3] Sun, R.; Duan, Z. An accurate model to predict the thermodynamic stability of methane hydrate and methane solubility in marine environments. *Chem. Geol.* **2007**, *244*, 248-262.
- [4] Sloan, E. D. Physical/chemical properties of gas hydrates and application to world margin stability and climatic change. *J. Vac. Sci. Technol.* **1998**, *137*, 31-50.
- [5] Warriar, P.; Khan, M.N.; Srivastava, V.; Maupin, C. M.; Koh, C. A. Overview: Nucleation of clathrate hydrates. *J. Chem. Phys.* **2016**, *145*, 211705.
- [6] Cygan, R. T.; Guggenheim, S.; Koster, van. Groos. A. F. Molecular models for the intercalation of methane hydrate complexes in montmorillonite clay. *J. Phys. Chem. B.* **2004**, *108*, 15141-15149.
- [7] Saw, V. K.; Udayabhanu, G. N.; Mandal, A.; Laik, S. Methane Hydrate Formation and Dissociation in the presence of Bentonite Clay Suspension. *Chem. Eng. Technol.* **2013**, *36*, 810-818.
- [8] Uchida, T.; Takeya, S.; Chuvilin, E. M.; Ohmura, R.; Nagao, J.; Yakushev, V. S.; Nanrita, H. Decomposition of methane hydrates in sand, sandstone, clays, and glass beads. *J. Geophys. Res.: Solid Earth.* **2004**, *109*. B05206.
- [9] Lamorena, R. B.; Woojin, L. Formation of carbon dioxide hydrate in soil and soil mineral suspensions with electrolytes. *Environ. Sci. Technol.* **2008**, *42*, 2753-2759.
- [10] Young-ju, J. S.; Sun-Hwa, Yeon. Structural, Mineralogical, and Rheological Properties of Methane Hydrates in Smectite Clays. *J. Chem. Eng. Data.* **2009**, *54*, 1284-1291.
- [11] Yeon, S. H.; Seol, J.; Seo, Y. J.; Park, Y.; Koh, D. Y.; Park, K. P.; Lee, H. Effect of interlayer ions on methane hydrate formation in clay sediments. *J. Phys. Chem. B.* **2009**, *113*, 1245-1248.
- [12] Choudhary, N.; Hande, V. R.; Roy, S.; Chakrabarty, S.; Kumar, R. Effect of Sodium Dodecyl Sulfate Surfactant on Methane Hydrate Formation: A Molecular Dynamics Study. *J. Phys. Chem. B.* **2018**, *122*, 6536-6542.
- [13] Veluswamy, H. P.; Pei, Y. L.; Premasinghe, K.; Linga, P. Effect of Biofriendly Amino Acids on the Kinetics of Methane Hydrate Formation and Dissociation. *Ind. Eng. Chem. Res.* **2017**, *56*, 6145-6154.

- 1
2
3
4 [14] Sa, J. H.; Kwak, G. H.; Han, K.; Ahn, D.; Cho, S. J.; Ju, D. L.; Lee, H. Inhibition of methane and
5 natural gas hydrate formation by altering the structure of water with amino acids. *Sci. Rep.* **2016**, *6*,
6 31582.
7
8
9 [15] Wu, G.; Ji, H.; Tian, L.; Chen, D. Effects of Salt Ions on the Methane Hydrate Formation and
10 Dissociation in the Clay Pore Water and Bulk Water. *Energy Fuels.* **2018**, *32*, 12486-12494.
11
12 [16] Kim, D.; Ahn, Y. H.; Kim, S. J.; Lee, J. Y.; Lee, J.; Seo, Y. J.; Lee, H. Gas Hydrate in
13 Crystalline-Swelled Clay: The Effect of Pore Dimension on Hydrate Formation and Phase Equilibria. *J.*
14 *Phys. Chem. C.* **2015**, *119*, 22148-22153.
15
16 [17] Guggenheim, S.; Koster van Groos, A. F. New gas-hydrate phase: Synthesis and stability of
17 clay-methane hydrate intercalate. *Geology.* **2003**, *31*, 653-656.
18
19 [18] Clennell, M. B.; Henry, P.; Hovland, M.; Booth, J. S.; Thomas, M. Formation of Natural Gas
20 Hydrates in Marine Sediments: Gas Hydrate Growth and Stability Conditioned by Host Sediment
21 Properties. *Ann. N. Y. Acad. Sci.* **1999**, *912*, 887-896.
22
23 [19] Martín-Puertas, C.; Mata, M.; Fernández-Puga, M.; del Río, V. D.; Vázquez, J.; Somoza, L. A
24 comparative mineralogical study of gas-related sediments of the Gulf of Cádiz. *Geo-Mar. Lett.* **2007**,
25 *27*, 223-235.
26
27 [20] Cha, S.; Ouar, H.; Wildeman, T.; Sloan, E. A third-surface effect on hydrate formation. *J. Phys.*
28 *Chem.* **1988**, *92*, 6492-6494.
29
30 [21] Zhou, Q.; Lu, X.; Liu, X.; Zhang, L.; He, H.; Zhu, J.; Yuan, P. Hydration of methane intercalated
31 in Na-smectites with distinct layer charge: Insights from molecular simulations. *J. Colloid Interface Sci.*
32 **2011**, *355*, 237-242.
33
34 [22] Bergaya, F.; Lagaly, G. Handbook of clay science. Volume 1. *Elsevier*, Amsterdam.
35 Developments of Clay Science. **2013**, 23-25.
36
37 [23] Liu, D.; Yuan, P.; Liu, H.; Cai, J.; Qin, Z.; Tan, D.; Zhu, J. Influence of heating on the solid
38 acidity of montmorillonite: A combined study by DRIFT and Hammett indicators. *Appl. Clay Sci.* **2011**,
39 *52*, 358-363.
40
41 [24] Park, S. H.; Sposito, G. Do Montmorillonite Surfaces Promote Methane Hydrate Formation?
42 Monte Carlo and Molecular Dynamics Simulations. *J. Phys. Chem. B.* **2003**, *107*, 2281-2290.
43
44 [25] Kotkoskie, T.; Al-Ubaidi, B.; Wildeman, T.; Sloan, E. Inhibition of gas hydrates in water-based
45 drilling muds. *SPE drilling engineering.* **1992**, *7*, 130-136.
46
47
48
49
50
51
52
53
54
55
56
57
58
59
60

- 1
2
3
4 [26] Park, T.; Kyung, D.; Lee, W. Effect of organic matter on CO₂ hydrate phase equilibrium in
5 phyllosilicate suspensions. *Environ. Sci. Technol.* **2014**, *48*, 6597-6603.
- 6
7 [27] Kim, D.; Lee, H. Phase behavior of gas hydrates in nanoporous materials: Review. *Korean J.*
8 *Chem. Eng.* **2016**, *33*, 1977-1988.
- 9
10 [28] Zheng, R. C.; Chan, A. H. M.; Babu, P.; Yang, M.; Linga, P. Effect of NaCl on methane hydrate
11 formation and dissociation in porous media. *J. Nat. Gas Sci. Eng.* **2015**, *27*, 178-189.
- 12
13 [29] Nguyen, N. N.; Nguyen, A. V. The dual effect of sodium halides on the formation of methane gas
14 hydrate. *Fuel.* **2015**, *156*, 87-95.
- 15
16 [30] Cha, M.; Hu, Y.; Sum, A. K. Methane hydrate phase equilibria for systems containing NaCl, KCl,
17 and NH₄Cl. *Fluid Phase Equilib.* **2016**, *413*, 2-9.
- 18
19 [31] Hensen, C.; Nuzzo, M.; Hornibrook, E.; Pinheiro, L. M.; Bock, B.; Magalhães, V. H.; Brückmann,
20 W. Sources of mud volcano fluids in the Gulf of Cadiz-indications for hydrothermal imprint. *Geochim.*
21 *Cosmochim. Acta.* **2007**, *71*, 1232-1248.
- 22
23 [32] Sun, X.; Mohanty, K. K. Kinetic simulation of methane hydrate formation and dissociation in
24 porous media. *Chem. Eng. Sci.* **2006**, *61*, 3476-3495.
- 25
26 [33] Wilder, J. W.; Seshadri, K.; Smith, D. H. Modeling Hydrate Formation in Media with Broad Pore
27 Size Distributions. *Langmuir.* **2001**, *17*, 6729-6735.
- 28
29 [34] Wang, H.; Chen, L.; Qu, Z.; Yin, Y.; Kang, Q.; Yu, B.; Tao, W. Q. Modeling of multi-scale
30 transport phenomena in shale gas production—a critical review. *Appl. Energy* **2020**, *262*, 114575.
- 31
32 [35] Wilder, J. W.; Seshadri, K.; Smith, D. H. Modeling Hydrate Formation in Media with Broad Pore
33 Size Distributions. *Langmuir.* **2001**, *17*, 6729-6735.
- 34
35 [36] Titiloye, J. O.; Skipper, N. T. Molecular dynamics simulation of methane in sodium
36 montmorillonite clay hydrates at elevated pressures and temperatures. *Mol. Phys.* **2001**, *99*, 899-906.
- 37
38 [37] Lee, J. H.; Guggenheim, S. Single crystal X-ray refinement of pyrophyllite-1 Tc. *Am. Mineral.*
39 **1981**, *66*, 350-357.
- 40
41 [38] Downs, R. T.; Hall-Wallace, M. The American Mineralogist crystal structure database. *Am.*
42 *Mineral.* **2003**, *88*, 247-250.
- 43
44 [39] Loewenstein, W. The distribution of aluminum in the tetrahedra of silicates and aluminates. *Am.*
45 *Mineral.* **1954**, *39*, 92-96.
- 46
47 [40] Li, X.; Li, H.; Yang, G. Configuration, anion-specific effects, diffusion, and impact on counterions
48
49
50
51
52
53
54
55
56
57
58
59
60

1
2
3
4 for adsorption of salt anions at the interfaces of clay minerals. *J. Phys. Chem. C.* **2016**, *120*,
5 14621-14630.

6
7 [41] Zhang, L.; Lu, X.; Liu, X.; Yang, K.; Zhou, H. Surface wettability of basal surfaces of clay
8 minerals: Insights from molecular dynamics simulation. *Energy Fuels.* **2016**, *30*, 149-160.

9
10 [42] Bhattacharjee, G.; Choudhary, N.; Kumar, A.; Chakrabarty, S.; Kumar, R. Effect of the amino acid
11 l-histidine on methane hydrate growth kinetics. *J. Nat. Gas Sci. Eng.* **2016**, *35*, 1453-1462.

12
13 [43] Jiménez-Ángeles, F.; Firoozabadi, A. Nucleation of methane hydrates at moderate subcooling by
14 molecular dynamics simulations. *J. Phys. Chem. C.* **2014**, *118*, 11310-11318.

15
16 [44] Hess, B.; Kutzner, C.; Van, S. D.; Lindahl, E. GROMACS 4: algorithms for Highly Efficient,
17 Load-Balanced, and Scalable Molecular Simulation. *J. Chem. Theory Comput.* **2008**, *4*, 435-447.

18
19 [45] Cygan, R. T.; Liang, J. J.; Kalinichev, A. G. Molecular Models of Hydroxide, Oxyhydroxide, and
20 Clay Phases and the Development of a General Force Field. *J. Phys. Chem. B.* **2004**, *108*, 1255-1266.

21
22 [46] Jorgensen, W. L.; Madura, J. D.; Swenson, C. J. Optimized intermolecular potential functions for
23 liquid hydrocarbons. *J. Am. Chem. Soc.* **1984**, *106*, 6638-6646.

24
25 [47] Abascal, J. L. F.; Sanz, E.; Fernández, R.; García, Vega. C. A potential model for the study of ices
26 and amorphous water: TIP4P/Ice. *J. Chem. Phys.* **2005**, *122*, 268-342.

27
28 [48] Allen, M. P.; Tildesley, D. J. Computer simulation of liquids. *Oxford university press*, **2017**.

29
30 [49] Darden, T.; York, D.; Pedersen, L. Particle mesh Ewald: An $N \cdot \log(N)$ method for Ewald sums in
31 large systems. *J. Chem. Phys.* **1993**, *98*, 10089-10092.

32
33 [50] Evans, D. J.; Holian, B. L. The nose-hoover thermostat. *J. Chem. Phys.* **1985**, *83*, 4069-4074.

34
35 [51] Parrinello, M.; Rahman, A. Polymorphic transitions in single crystals: A new molecular dynamics
36 method. *J. Appl. Phys.* **1981**, *52*, 7182-7190.

37
38 [52] Walsh, M. R.; Koh, C. A.; Dendy, S.; Sum, A. K.; Wu, D. T. Microsecond simulations of
39 spontaneous methane hydrate nucleation and growth. *Science.* **2009**, *326*, 1095-1098.

40
41 [53] Jenel, V.; Kusalik, P. G. Unusual crystalline and polycrystalline structures in methane hydrates. *J.*
42 *Am. Chem. Soc.* **2006**, *128*, 15588-15589.

43
44 [54] Makov, G.; Payne, M. Periodic boundary conditions in ab initio calculations. *Phys. Rev. B.* **1995**,
45 *51*, 4014-4022.

46
47 [55] Baez, L. A.; Clancy, P. Computer Simulation of the Crystal Growth and Dissolution of Natural
48 Gas Hydrates. *Ann. N. Y. Acad. Sci.* **1994**, *715*, 177-186.

- 1
2
3
4 [56] Rodger, P.; Forester, T.; Smith, W. Simulations of the methane hydrate/methane gas interface near
5 hydrate forming conditions conditions. *Fluid phase equilibria*. **1996**, *116*, 326-332.
6
7 [57] Moon, C.; Hawtin, R.; Rodger, P. M. Nucleation and control of clathrate hydrates: insights from
8 simulation. *Faraday Discuss.* **2007**, *136*, 367-382.
9
10 [58] Jiménez-Ángeles, F.; Firoozabadi, A. Enhanced hydrate nucleation near the limit of stability. *J.*
11 *Phys. Chem. C*. **2015**, *119*, 8798-8804.
12
13 [59] Jacobson, L. C.; Hujo, W.; Molinero, V. Thermodynamic stability and growth of guest-free
14 clathrate hydrates: a low-density crystal phase of water. *J. Phys. Chem. B*. **2009**, *113*, 10298-10307.
15
16 [60] Ji, H.; Chen, D.; Chen, Z.; Wu, G. Molecular Dynamics Simulation of Methane Hydrate
17 Formation and Dissociation in the Clay Pores With Fatty Acids. *J. Phys. Chem. C*. **2017**, *122*,
18 1318-325.
19
20 [61] Guo, G. J.; Rodger, P. M. Solubility of aqueous methane under metastable conditions:
21 implications for gas hydrate nucleation. *J. Phys. Chem. B*. **2013**, *117*, 6498-6504.
22
23 [62] Walsh, M. R.; Beckham, G. T.; Koh, C. A.; Sloan, E. D.; Wu, D. T.; Sum, A. K. Methane hydrate
24 nucleation rates from molecular dynamics simulations: Effects of aqueous methane concentration,
25 interfacial curvature, and system size. *J. Phys. Chem. C*. **2011**, *115*, 21241-21248.
26
27 [63] Zhang, Z.; Walsh, M. R.; Guo, G. J. Microcanonical molecular simulations of methane hydrate
28 nucleation and growth: Evidence that direct nucleation to sI hydrate is among the multiple nucleation
29 pathways. *Phys. Chem. Chem. Phys.* **2015**, *17*, 8870-8876.
30
31 [64] Jacobson, L. C.; Hujo, W.; Molinero, V. Amorphous precursors in the nucleation of clathrate
32 hydrates. *J. Am. Chem. Soc.* **2010**, *132*, 11806-11811.
33
34 [65] Sarupria, S.; Debenedetti, P. G. Homogeneous Nucleation of Methane Hydrate in Microsecond
35 Molecular Dynamics Simulations. *J. Phys. Chem. Lett.* **2012**, *3*, 2942-2947.
36
37 [66] Yeon, S. H.; Seol, J.; Koh, D. Y.; Seo, Y. J.; Lee, H. Abnormal methane occupancy of natural gas
38 hydrates in deep sea floor sediments. *Energy Environ. Sci.* **2011**, *4*, 421-424.
39
40 [67] Koh, C. A.; Wisbey, R. P.; Wu, X.; Westacott, R. E.; Soper, A. K. Water ordering around methane
41 during hydrate formation. *J. Chem. Phys.* **2000**, *113*, 6390-6397.
42
43 [68] Chialvo, A. A.; Houssa, M.; Cummings, P. T. Molecular Dynamics Study of the Structure and
44 Thermophysical Properties of Model sI Clathrate Hydrates. *J. Phys. Chem. B*. **2002**, *106*, 442-451.
45
46 [69] Chun-Yu, G.; Hao, W.; Han, Z. Molecular simulation of the potential of methane reoccupation
47
48
49
50
51
52
53
54
55
56
57
58
59
60

- 1
2
3
4 during the replacement of methane hydrate by CO₂. *J. Phys. Chem. A*. **2009**, *113*, 5463-5469.
- 5
6 [70] Teich-Mcgoldrick; S. L.; Greathouse, J. A.; Jové-Colón, C. F.; Cygan, R. T. Swelling Properties
7 of Montmorillonite and Beidellite Clay Minerals from Molecular Simulation: Comparison of
8 Temperature, Interlayer Cation, and Charge Location Effects. *J. Phys. Chem. C*. **2015**, *119*,
9 20880-20891.
- 10
11
12 [71] Li, X.; Li, Q.; Yang, S.; Yang, G. Swelling of Clay Minerals: Dual Characteristics of K⁺ ions and
13 Exploration for Critical Influence Factor. *Phys. Chem. Chem. Phys.* **2019**, *21*, 1963-1971.
- 14
15 [72] Zhang, L.; Lu, X.; Liu, X.; Zhou, J.; Zhou, H. Hydration and Mobility of Interlayer Ions of (Na_x,
16 Ca_y)-Montmorillonite: A Molecular Dynamics Study. *J. Phys. Chem. C*. **2014**, *118*, 29811-29821.
- 17
18 [73] Breslow, R. Hydrophobic Effects on Simple Organic Reactions in Water. *Acc. Chem. Res.* **1991**,
19 22, 159-164.
- 20
21 [74] Jiménez-Ángeles, F.; Firoozabadi, A. Hydrophobic Hydration and the Effect of NaCl Salt in the
22 Adsorption of Hydrocarbons and Surfactants on Clathrate Hydrates. *ACS Cent. Sci.* **2018**, *4*, 820-831.
- 23
24 [75] Yan, K. F.; Li, X. S.; Chen, Z. Y.; Xia, Z. M.; Xu, C. G.; Zhang, Z. Molecular dynamics
25 simulation of the crystal nucleation and growth behavior of methane hydrate in the presence of the
26 surface and nanopores of porous sediment. *Langmuir*. **2016**, *32*, 7975-7984.
- 27
28 [76] Jorgensen, W.; Madura, J. Temperature and size dependence for Monte Carlo simulations of
29 TIP4P water. *Mol. Phys.* **2015**, *56*, 1381-1392.
- 30
31 [77] Chang, F. R. C. Monte Carlo and Molecular Dynamics Simulations of Interfacial Structure in
32 Lithium-Montmorillonite Hydrates. *Langmuir*. **1997**, *13*, 2074-2082.
- 33
34 [78] Varma, S.; Rempe, S. B. Coordination numbers of alkali metal ions in aqueous solutions. *Biophys.*
35 *Chem.* **2006**, *124*, 192-199.
- 36
37
38
39
40
41
42
43
44
45
46
47
48
49
50
51
52
53
54
55
56
57
58
59
60

Table of Content

